Applied Physics A (2023) 129:100
https://doi.org/10.1007/s00339-022-06366-3

Applied Physics A
Materials Science & Processing

Investigation of electrical properties of Al/$LiCoO_2$/*n*-Si photodiode by ultrasonic spray pyrolysis method

Ali Akbar Hussaini[1,2] · Mehmet Okan Erdal[3] · Kemal Doğan[4] · Mustafa Koyuncu[5] · Murat Yildirim[1]

Received: 15 October 2022 / Accepted: 25 December 2022 / Published online: 11 January 2023

Abstract
There has been rising concentration on the photodiode properties of the MS devices in recent years to improve the performance of light sensing devices. Therefore, in this study, $LiCoO_2$ was synthesized via sol–gel-based electrospinning method and it is used as interlayer between Al and *n*-type Si to fabricate Al/$LiCoO_2$/*n*-Si photodiode via ultrasonic spray pyrolysis and physical vapor deposition methods. $LiCoO_2$ thin film was characterized via XRD, SEM and AFM. Crystallite size for $LiCoO_2$ was found to be 37.75 nm. Electrical characterization was performed by current–voltage ($I-V$) and current-transient ($I-t$) measurements using solar simulator under dark and various illumination conditions. $I-V$ characteristics demonstrated that the Al/$LiCoO_2$/*n*-Si exhibited good photodiode behavior and a high rectifying ratio. Moreover, $LiCoO_2$-interlayered device has shown significant responsivity and detectivity. It has shown 1.79×10^{10} Jones detectivity and 0.364 A/W responsivity at 100 mW light power. Thus, the results demonstrate that a device based on $LiCoO_2$ can be employed in optoelectronic applications.

Keywords $LiCoO_2$ · Photodiode · Ultrasonic spray pyrolysis

1 Introduction

Advances in the electronic industry have created a great demand for new functional materials which possess particular native properties and functions of their own. Semiconductors, dielectrics, ferroelectrics, polymers, molecular crystals, nanoparticles, etc., are good examples of functional materials. Metal–semiconductor (MS) contacts are crucial to the operation of all semiconductor devices and integrated circuits. Many scientists are therefore attracted to MS structures due to their signification in electronics such as capacitors, diodes, transistors, photodetectors, and solar cells [1–7]. MS structures can be performed as photodiode or photodetector at the reverse biases [8]. Photodetectors are the devices which can convert optical signals to electronic signals via the photoelectric effect [9]. Photodetectors are essential for many scientific and industrial applications, including image sensing, optical communications, environmental monitoring, chemical and biological sensing, monitoring manufacturing processes, smart phones, self-driving cars, unmanned aerial vehicles, distance detectors, alarm systems, and so on [10–14]. Photo-detecting technologies can be categorized into distinct groups, such as photodiodes, photoconductors, or phototransistors, depending on their underlying operating principles or device architecture. The photodiodes are able to produce photocurrent by directly converting light into extractable charges. After light has been absorbed, photoactive materials' conductance can alter in photoconductors, and light absorption can control the channel's conductance between its source and drain in phototransistors [15].

In recent years, to enhance the performance of light sensing, several researchers have concentrated on the photodiode

✉ Ali Akbar Hussaini
aliakbar.hussaini.1994@gmail.com

✉ Murat Yildirim
muratyildirim@selcuk.edu.tr

[1] Department of Biotechnology, Faculty of Science, Selcuk University, 42130 Konya, Turkey

[2] Department of Biotechnology and Food Microbiology, Faculty of Biotechnology and Food Science, Wrocław University of Environmental and Life Sciences, 51630 Wrocław, Poland

[3] Meram Vocational School, Necmettin Erbakan University, 42090 Konya, Turkey

[4] Department of Nanotechnology and Advanced Materials, Institute of Science, Selcuk University, 42130 Konya, Turkey

[5] Department of Physics, Faculty of Science, Selcuk University, 42130 Konya, Turkey

features of the MS devices. Therefore, great effort has been put into obtaining effective photodiodes with various interface layers such as metal oxides, polymers or insulators prepared by sophisticated techniques [16–20]. In the literature, various types of materials such as ZnO, NiO, CdO, TiO_2, SiO_2, V_2O_5, Ga_2O_3, and $BaTiO_3$, various polymers, etc., have been used as an interfacial layer for photodiode fabrication [21, 22].

There are various low-cost thin-film coating techniques, including dip coating, spin coating, spray coating, blade coating, and roll coating [23]. Moreover, ultrasonic spray pyrolysis (USP) technique is a droplet production phenomenon brought on by ultrasonic waves. It has a number of intriguing characteristics, such as simplicity, cost-effectiveness, continuous operation, rapid deposition rate, and the capacity to deposit on large surface regions. Additionally, USP features the highly desirable capability of multilayer preparation for creating functionally graded layers [24].

$LiCoO_2$ is a *p*-type semiconductor with 2.7 eV bandgap energy which has been applied in rechargeable lithium-ion batteries, and could have applicability in other areas such as UV photodetectors and photocatalyst [25].

The electrospinning approach based on sol–gel is a versatile way to make nanofibers, and in recent years, it has been widely employed to fabricate nanocomposite materials. In comparison with standard sol–gel processes, which typically yield powders in the range of 1–3 mm, Ou et al. developed dried and ground the $LiCoO_2$/poly(vinyl pyrrolidone) (PVP) nanofibers into powders and obtained ultrafine $LiCoO_2$ powders with excellent electrochemical behaviors under lower calcination temperature and shorter calcination time [26]. It has been found that nanoparticles synthesized via electrospinning are consisting of smaller particles and their electrical properties are more improved [27]. Therefore, in this present study, we synthesized $LiCoO_2$ nanofibers via the sol–gel-based electrospinning method. Electrospun $LiCoO_2$ nanofibers were calcinated at 650 °C at a heating rate of 10 °C/min. Calcinated $LiCoO_2$ was ball-milled and applied as interlayer in Al/$LiCoO_2$/*n*-Si structure via ultrasonic spray pyrolysis. Current–voltage ($I-V$) and current-transient ($I-t$) measurements were performed to investigate the electrical properties of the fabricated device.

2 Experimental

2.1 Materials

Polyvinylpyrrolidone (PVP) with a molecular weight of 1,300,000 was purchased from Alfa Aesar. Cobalt (II) acetate tetrahydrate ($(CH_3COO)_2$ $Co{\cdot}4H_2O$) with 249.08 molecular weight and 99.95% high-purity lithium acetate with molar mass of 65.99 g/mol were purchased from Sigma-Aldrich. For the cleaning procedure, hydrofluoric acid (HF, 48%), isopropyl alcohol ($(CH_3)_2CHOH, \geq 99.7\%$), and acetone ($CH_3COCH_3, \geq 99.5\%$) were purchased from Merck. A phosphorus-doped Si wafer with (111) orientation, 1–20 Ω cm resistivity and 500–550 µm thickness was purchased from Wafer World. Aluminum (Al, 99.9%) and silver (Ag, 99.9%) were supplied from Sigma-Aldrich to obtain ohmic and metallic contacts, respectively.

2.2 Synthesis of $LiCoO_2$ and electrospinning of $LiCoO_2$ nanofiber

In this study, it is aimed to prepare $LiCoO_2$ powder from lithium acetate and cobalt acetate powders. Lithium acetate (99.95%) with molar mass of 65.99 g/mol and cobalt(II) acetate tetrahydrate with molar mass of 249.08 g/mol were dissolved in deionized water at ¼ rate on magnetic stirrer to synthesize $LiCoO_2$. Then the solution was added to 10% PVP polymer solution. Electrospinning was carried out at a voltage of 10–12 kV, the distance between the syringe and the top of the syringe was 12–14 cm, and the pump speed was 1 µl/min. The obtained fibers were put into the curing oven in the crucible for removal of polymers and oxidation. Curing was carried out at 650 °C at a heating rate of 10 °C/min. After calcination, the powders were ball milled in a mechanical mixer at 350 rpm for 1 h to obtain a homogeneous structure.

2.3 Device fabrication

Si wafers were cleaned via RCA cleaning procedure [28]. Moreover, they were treated with HF/H_2O (1:10) to eliminate the impurities. Afterward, they were transferred to a thermal evaporator to create ohmic contacts. 100 nm Al was deposited on the back surface of Si wafers at 5×10^{-6} Torr. Then, they were treated with 500 °C temperature in N_2 atmosphere for 5 min. Calcinated $LiCoO_2$ was added to distilled water (5 g L^{-1} concentration) and then put onto a magnetic stirrer for 1 h. $LiCoO_2$ solution was deposited on the front surface of the wafer via ultrasonic spray pyrolysis. 5 ml of the $LiCoO_2$ solution was placed in an ultrasonic nebulizer vibrated at a frequency of 50 kHz. Ultrasonic spray was performed as the nozzle moved on the hot plate annealed at 200 °C, gap between plate and nozzle was arranged to 3 cm, and spray rate was 25 mL h^{-1}. To form metallic contact, Ag was evaporated on $LiCoO_2$ surface by a 1-mm hole array mask. The pressure in the thermal evaporator was 5×10^{-6} Torr. The schematic illustration of the obtained heterojunction is shown in Fig. 1. As can be seen from inset, Ag metallic contact was formed successfully and measured as ~ 2.1 mm by ImageJ program. Moreover, in order not to harm the contacts during measurements, copper wire was connected by silver paste.

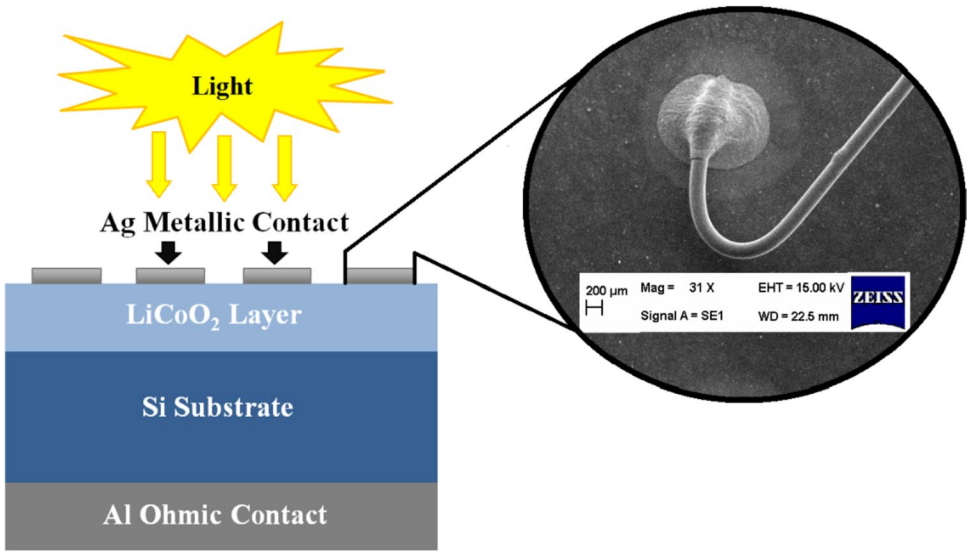

Fig. 1 Schematic illustration of Al/$LiCoO_2$/*n*-Si and SEM image of it from top

3 Results and discussion

3.1 Morphological and structural analysis

To investigate the surface morphology of the $LiCoO_2$ nanofibers, nanoparticles and nanofilm, scanning electron microscopy (SEM) was used. $LiCoO_2$ nanofibers show homogeneous distribution and are randomly aligned with average widths of 3500–4000 nm, shown in Fig. 2a, b. Fibers are almost at the same diameter, and there is no trace of droplets in fibers. Furthermore, there are no signs of nanoparticles on the surface of fibers. SEM images of $LiCoO_2$ structure after calcination are shown in Fig. 2c. As can be seen from Fig. 2c, no trace of fibers can be observed and crystal structures were measured via ImageJ application. Sphere-like structures were mostly between 257 and 415 nm, and average diameter was 345.6 nm. On the other hand, rod-like structures were measured and average length and diameter were 3396 nm and 778 nm, respectively. To obtain homogeneous structure, $LiCoO_2$ were ball-milled. As can be seen from Fig. 2d, it is irregularly shaped. $LiCoO_2$ was deposited on Si wafer and is shown in Fig. 2e. Diameter of particles was measured via ImageJ, shown in Fig. 2f. Particles were between 148 and 1062 nm and have average particles size of 324 nm.

$LiCoO_2$ powder was investigated by SEM–EDX morphologically. Figure 3 displays the SEM–EDX of the $LiCoO_2$ for a large surface area. The $LiCoO_2$ has nearly uniform surface area. It contains silicon (Si) due to substrate. Cobalt and oxygen atoms have been distributed homogeneously.

Further investigation on the surface morphology of $LiCoO_2$ film was conducted with atomic force microscopy (AFM) characterization (Fig. 4). AFM is the best tool for observing the surface texture of the deposited film and detecting the nanometric surface roughness quantitatively. The advantage of smooth surface is that interface traps and scattering centers are suppressed. Due to their smoother surface and compatibility with other junctions, thin films with decreased roughness can therefore be advantageous. Thin films with reduced roughness may consequently be useful due to their smoother surface and compatibility with other junctions [29, 30]. The photoresponse and photoelectric properties of the device can also be impacted by surface roughness [19]. Additionally, the smoother surface will produce a uniform electric field throughout the entire system. The direct tunneling current can be reduced, and photodiode characteristics can be improved by this uniform electric field [31]. As can be seen from Fig. 4, the surface of $LiCoO_2$ film has the shape of the hills and valleys. The root mean square (RMS) surface roughness value was 48.532 nm within the 5×5 µm^2 area, which demonstrates a quite uniform surface of the $LiCoO_2$ film. As can be seen from AFM image, particles were not distributed homogenously and heights of particles were up to 200 nm. This is consistent with results found from the SEM measurements.

$LiCoO_2$ was characterized by X-ray powder diffraction (XRD) to obtain information related to unit cell dimensions and phase identification of crystalline materials. As shown in the XRD pattern, peaks were located at $2\theta = 16.37$, 19.01, 31.46, 36.87, 38.5, 44.84, 49.12, 59.40, 65.28, 68.68° correspond to (111), (003), (220), (101), (102), (104), (105), (107), (108), and (113) planes, respectively. As shown in Fig. 5, it displays distinct (003), (101), and (104) diffraction peaks, indicating that it possesses a normal six-square-phase layered structure [32]. Moreover, the intensity distribution of the (101), (006), (102), and (104) peaks shows clearly that

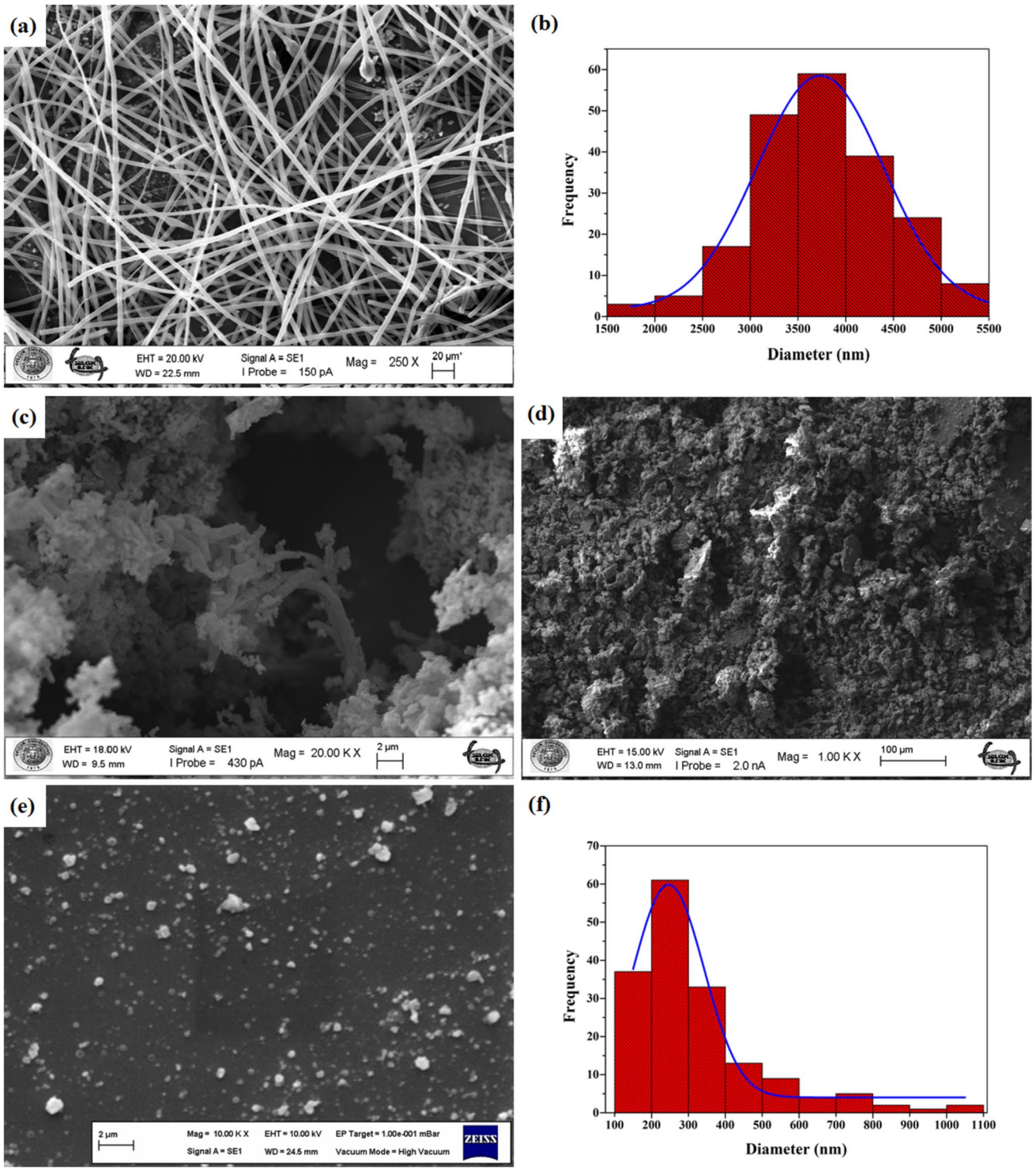

Fig. 2 **a** SEM image of $LiCoO_2$/PVP nanofiber, **b** histogram graphic of $LiCoO_2$/PVP nanofiber, **c** calcinated $LiCoO_2$, **d** ball-milled $LiCoO_2$, **e** $LiCoO_2$ complex on Si wafer, and **f** histogram graphic of $LiCoO_2$ particles

the Co ions do not occupy the Li sites [33, 34]. Moreover, peaks at (111) and (220) could be attributed to Co_3O_4 existence [35, 36].

The texture of the planes in the $LiCoO_2$ film is described numerologically by the texture coefficient ($TC_{(hkl)}$). The following relation provides the planes' ($TC_{(hkl)}$) coefficient values [37]:

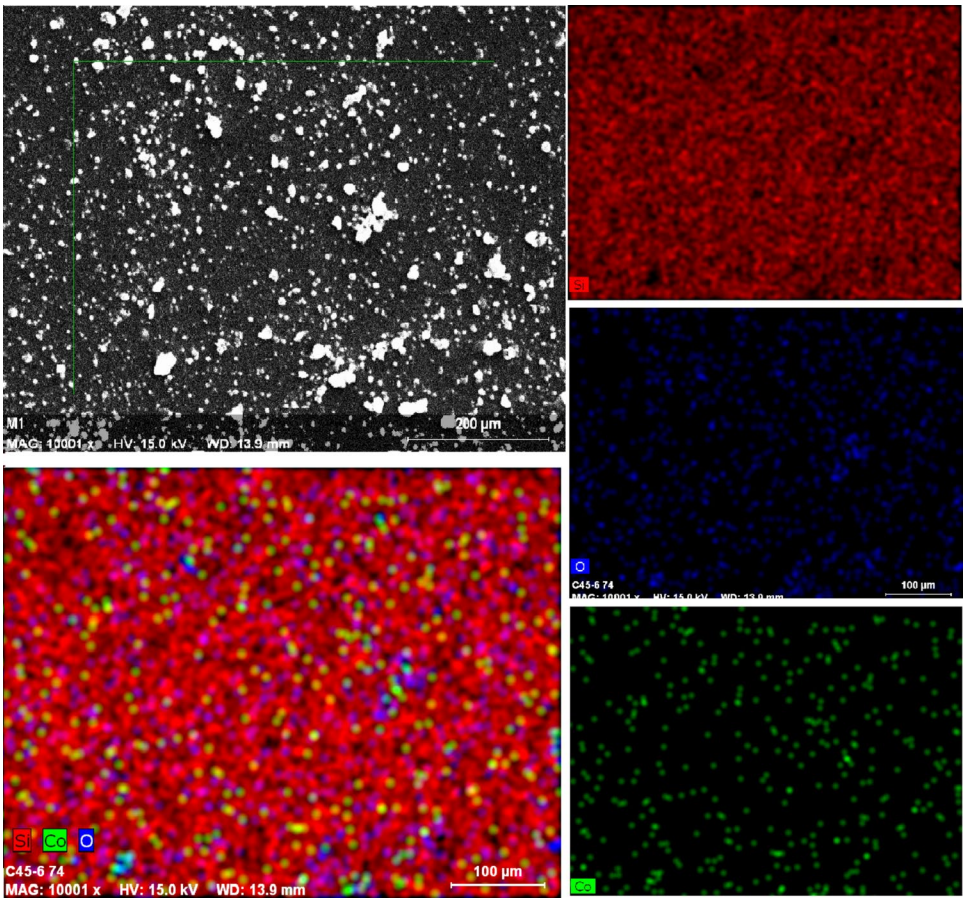

Fig. 3 SEM–EDX fast map analysis of $LiCoO_2$

$$TC_{(hkl)} = \frac{I_{(hkl)}/I_{0(hkl)}}{N^{-1}\sum_N I_{(hkl)}/I_{0(hkl)}} \quad (1)$$

here $I_{(hkl)}$ is the observed peak intensity, $I_{0(hkl)}$ is the standard reference intensity values of the *(hkl)* planes, and N is the total number of diffraction lines. The various planes' obtained *TC(hkl)* value are shown in Fig. 6. Intensity was 6943, 6810, 8983, 11,883, 10,370, 11,392, and 11,925 for (111), (003), (220), (101), (104), (107), and (108) planes, respectively.

The crystallite size (D), microstrain (ε), and dislocation density (ρ) values of the $LiCoO_2$ thin films were determined from XRD graphs via the following equations to explore the effects of the microstructural features [37]:

$$D = \frac{0.94\lambda}{\beta\cos\theta} \quad (2)$$

$$\varepsilon = \frac{\beta\cos\theta}{4} \quad (3)$$

$$\rho = \frac{15\varepsilon}{\alpha D} \quad (4)$$

here λ is the X-ray wavelength, β is the peak's FWHM value, and θ is the Bragg's diffraction angle. Lattice constant is considered as 14.05 Å for $LiCoO_2$. D, ε, and ρ values were calculated for (111), (003), (220), (101), (104), (107), and (108) planes. While mean crystallite size for $LiCoO_2$ was 37.75 nm, mean ε and ρ values were calculated as 1.141×10^{-3} and 4.417×10^{5} cm^{-2}, respectively.

3.2 Electrical properties

To determine the photodetection behaviors of the fabricated devices, Fytronix FY-7000 solar simulator was used under dark and various illuminations. ln$I$−V graphics are given in Fig. 7. It can be seen that forward currents increase with increasing light power with $LiCoO_2$ addition compared to Al/*n*-Si and slightly increase the reverse current values.

Rectifying ratio (RR) plots have been calculated using $RR = I_{forward}/I_{reverse}$ formula at ±3 V, and illustrated in Fig. 8. To compare the two devices, the highest RR value was obtained for $LiCoO_2$-interlayered device under dark conditions. Generally, the RR values of both devices were decreased by increasing illumination.

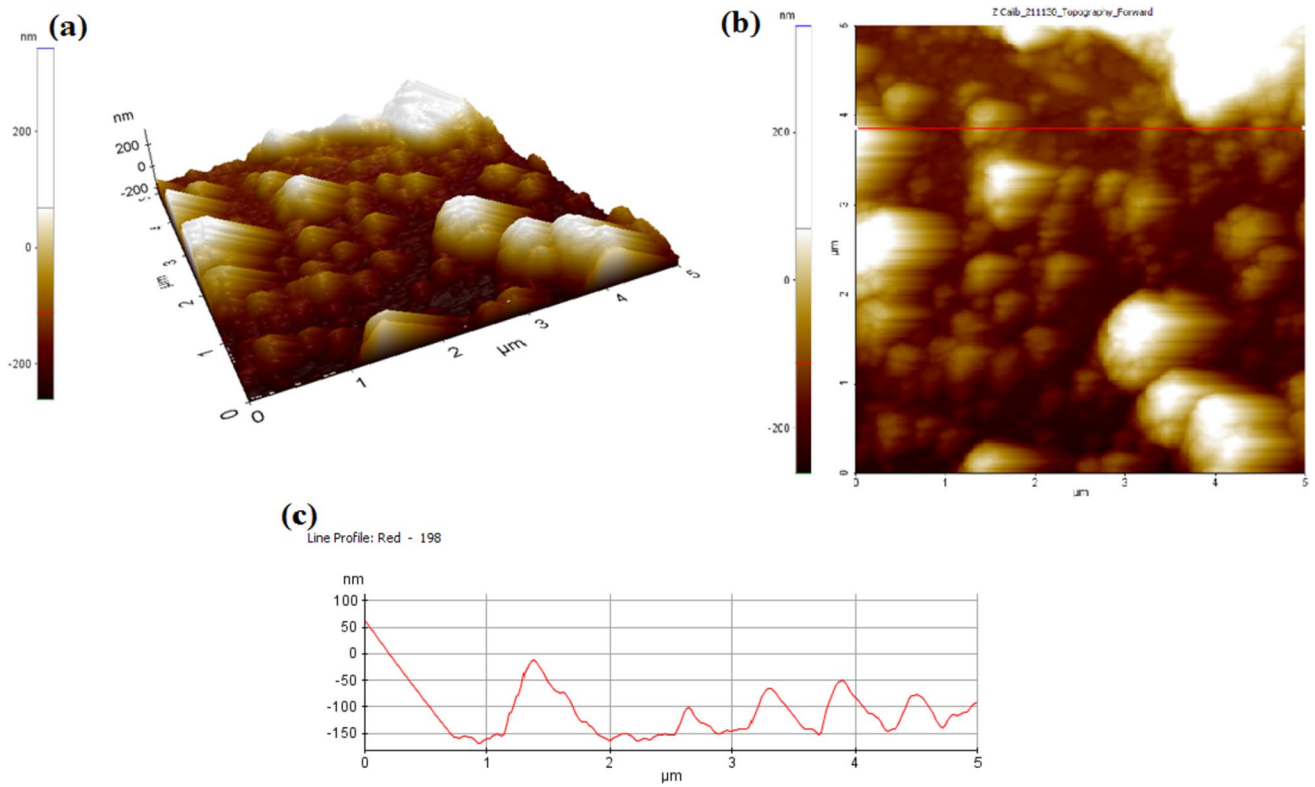

Fig. 4 **a** 3D, **b** 2D AFM images of $LiCoO_2$, and **c** line profile

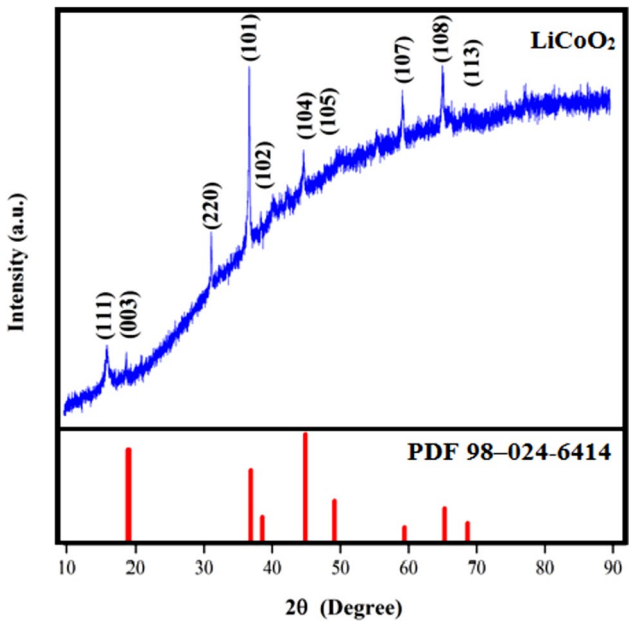

Fig. 5 XRD patterns for $LiCoO_2$ and Reference pattern for $LiCoO_2$ material (obtained from PDF 98-024-6414)

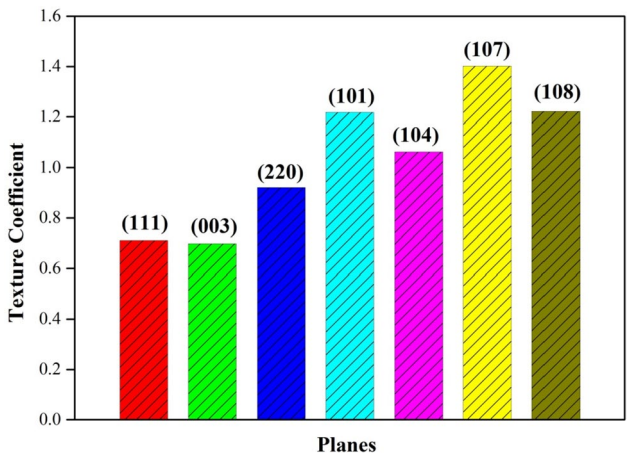

Fig. 6 The texture coefficient for (111), (003), (220), (101), (104), (107), and (108) planes of $LiCoO_2$ thin films

Diode parameters provide basic and particular information about the quality of diodes, and there are methods such as thermionic emission (TE), Norde and Cheung methods to calculate the ideality factor (n), series resistance (R_s) and barrier height (Φ_B). In Table 1, diode parameters of Al/n-Si and Al/$LiCoO_2$/n-Si devices are calculated and listed using above-mentioned methods. Saturation current, n and Φ_B of the Al/n-Si and $LiCoO_2$-interlayered devices are obtained via TE. According to the TE theory, $V > 3kT$ is assumed and the following equations can be used [38, 39]:

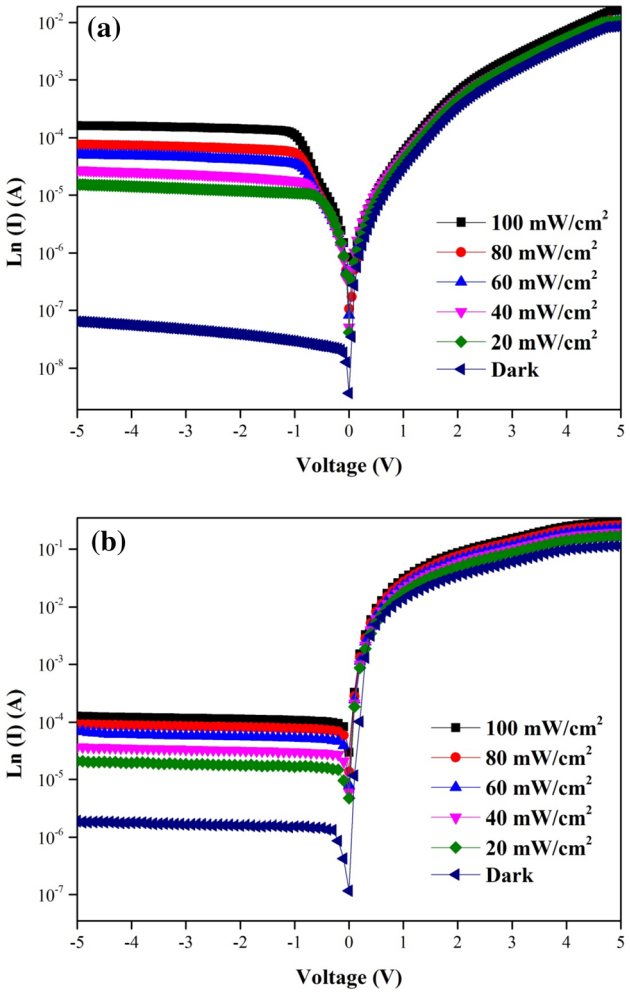

Fig. 7 ln *I–V* plots of the **a** undoped and **b** $LiCoO_2$-interlayered devices

$$I = I_0\left[\exp\left(\frac{qV}{nkT}\right) - 1\right];\ I_0 = AA^*T^2\exp\left(-\frac{q\Phi_B}{kT}\right) \quad (5)$$

here, I_0 corresponds to saturation current, q is electronic charge, A is contact area, A^* is Richardson constant (for n type silicon, $A^* = 120$ A cm^{-2} K^{-2}), and T is the absolute temperature. The n and Φ_B are calculated via the following equations for $V > 3kT/q$.

$$\Phi_B = \frac{kT}{q}\ln\left(\frac{AA^*T^2}{I_0}\right) \text{ and } n = \frac{q}{kT}\frac{dV}{\mathrm{d}}\ln(I) \quad (6)$$

Saturation currents were 4.02×10^{-7} and 3.88×10^{-5} A for undoped and $LiCoO_2$-interlayered photodiodes, respectively. n values were calculated as 5.41 and 1.97 for undoped and $LiCoO_2$-interlayered devices, respectively. Φ_B values were obtained according to I_0 values and were found as 0.675 eV and 0.556 eV for undoped and $LiCoO_2$-interlayered devices, respectively. Under different illumination intensities and dark conditions, n and Φ_B of the both devices were calculated and are illustrated in Fig. 9. As can be seen from Fig. 9, barrier height has been decreasing by increase in light intensity due to charge carriers increasing with illumination [40]. Furthermore, according to literature, the interfacial layer and lateral inhomogeneous Φ_B distributions are responsible for the large n values [41, 42].

According to Cheung's approach, the current is given by the following equation:

$$I = I_0\exp\left(-\frac{q(V - IR_s)}{nkT}\right) \quad (7)$$

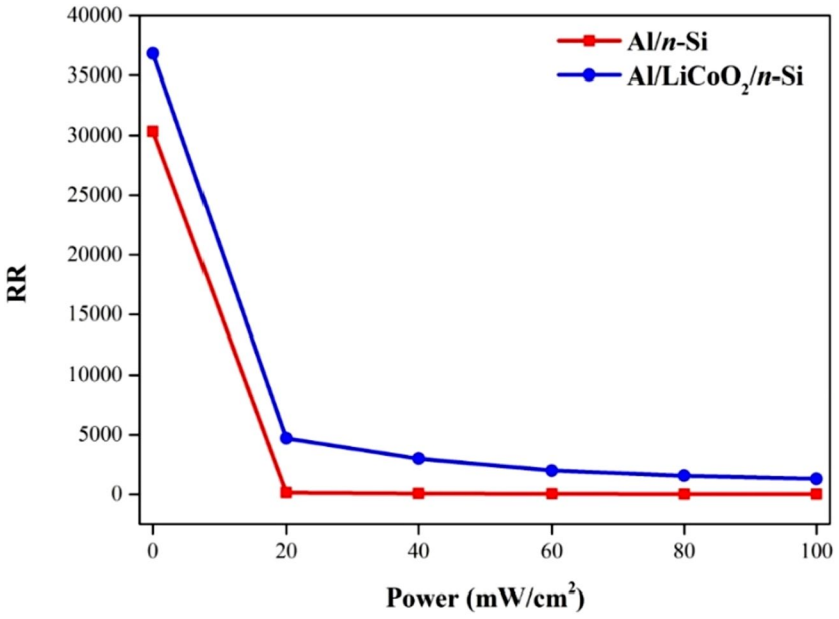

Fig. 8 Rectifying ratio graphics of the **a** undoped and **b** $LiCoO_2$-interlayered devices

Table 1 Diode parameters obtained by TE, Cheung, and Norde's approaches

Device	Saturation current (I_0)	n (I–V) –	n Cheung –	Φ_B(I–V) (eV)	Φ_B Cheung (eV)	Φ_B Norde (eV)	R_s Cheung (kΩ ($H(I)$))	R_s Cheung ((kΩ (dln(I)))	R_s Norde (kΩ)
Al/n-Si	4.02×10^{-7}	5.41	5.41	0.675	0.664	0.671	5.38	7.92	17.68
Al/$LiCoO_2$/n-Si	3.88×10^{-5}	1.97	1.93	0.556	0.557	0.554	0.02	0.03	0.003

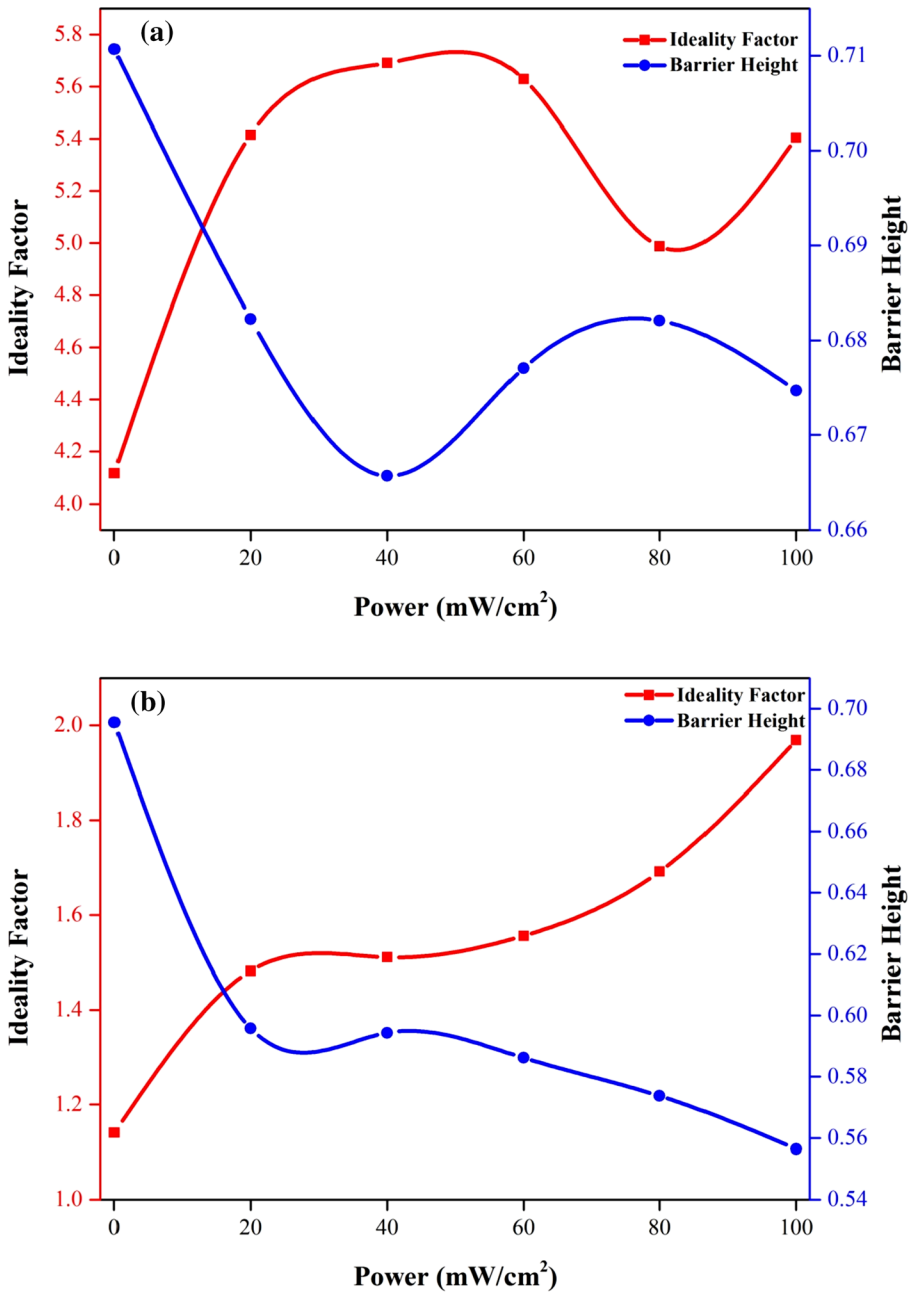

Fig. 9 n and Φ_B plots of the **a** undoped and **b** $LiCoO_2$-interlayered photodiodes

where IR_s is the voltage difference falling across the series resistance. The following relations can be obtained for the Cheung approximation:

$$\frac{dV}{d(\ln I)} = IR_s + n\frac{kT}{q} \tag{8}$$

$$H(I) = V - n\left(\frac{kT}{q}\right)\ln\left(\frac{I}{AA^*T^2}\right) \tag{9}$$

where $H(I)$ is rearranged:

$$H(I) = IR_s + n\Phi_B \tag{10}$$

If Eqs. (4) and (5) are plotted against current, the functions given above provide a linear variation of current. If the $dV/(d(\ln I)) - I$ change is plotted, R_s and $n\frac{kT}{q}$ can be calculated from the values where this graph cuts the slope and the y-axis, respectively. Φ_B and R_s value can be calculated using these values. However, if a graph of $H(I)$ versus I is drawn, Rs and $n\Phi_B$ values can be calculated from the point where this graph cuts the slope and y-axis, respectively [43]. The Cheung plots of the undoped and

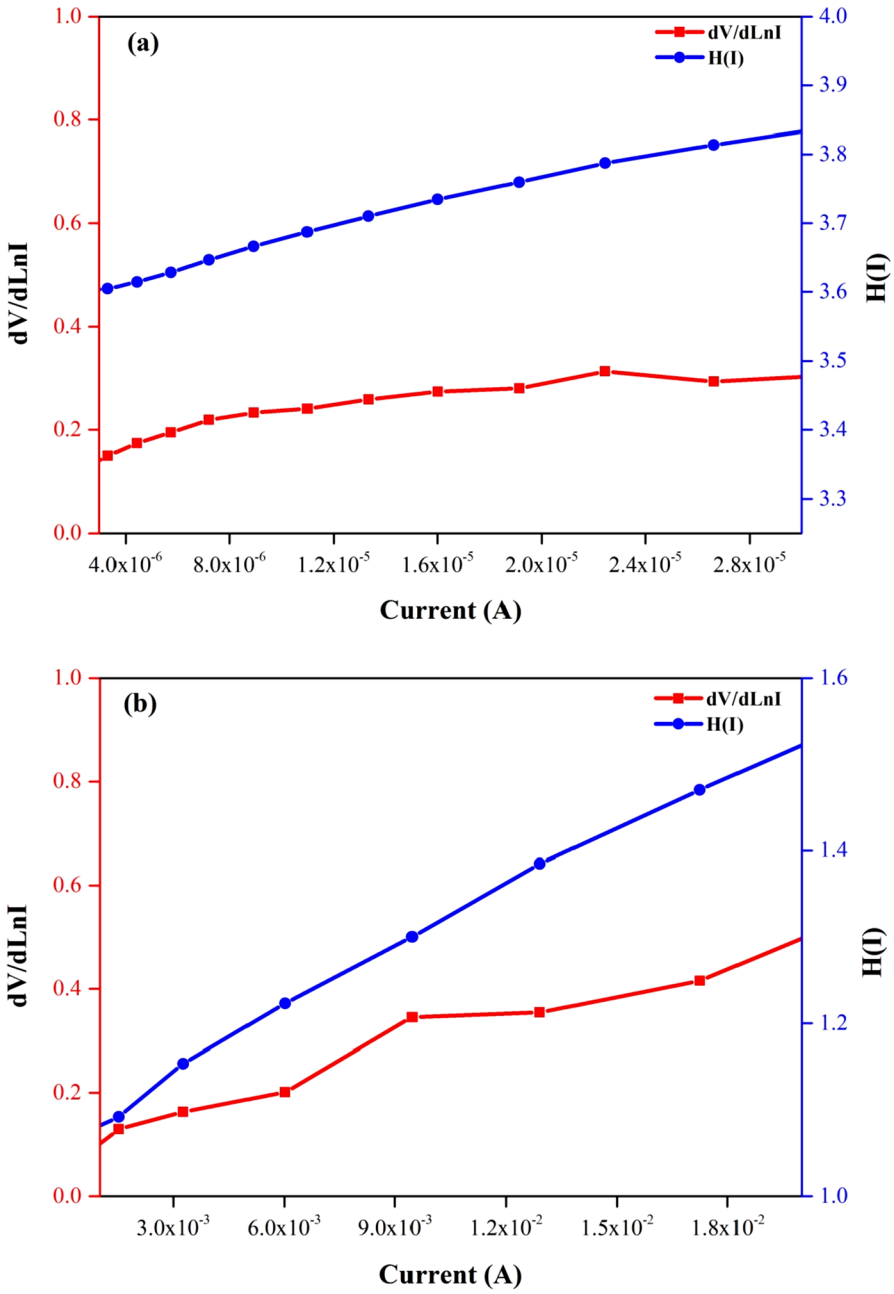

Fig. 10 Cheung plots of the **a** undoped and **b** $LiCoO_2$-interlayered photodiodes

$LiCoO_2$-interlayered devices are shown in Fig. 10. According to Table 1, calculated n and Φ_B are in a good harmony with the results obtained by all three methods. Moreover, the similarity of Rs values of both devices obtained by $dV/(d(\ln I)) - I$ and $H(I) - I$ graphics with each other verifies the consistency of Cheung method. Notably, there is a significant decrease in R_s values of the Al/$LiCoO_2$/n-Si device compared to Al/n-Si device.

Norde approximation is applicable for the applied voltages of ($V > 3kT/q$) [44]. To assure the precision of the calculations, Norde's approach is used. Barrier height and series resistance are calculated using Norde's approach as given in the following equations [45]:

$$F(V) = \frac{V}{\gamma} - \frac{kT}{q} \ln \frac{I(V)}{AA^*T^2} \tag{11}$$

where $I(V)$ is expressed voltage-dependent current and γ is the closest integer higher than the ideality factor. The Φ_B and R_s are calculated by the following equations:

$$\Phi B = F(V0) + \left[\frac{V_0}{\gamma} - \frac{kT}{q}\right] \tag{12}$$

and

$$R_s = \frac{\gamma - n}{I} \frac{kT}{q} \tag{13}$$

Here V_0 is the minimum voltage in the $F(V)$ graphics. Figure 11a, b shows the $F(V)$ versus V plots of the undoped and $LiCoO_2$-interlayered photodiodes, respectively. The calculated Φ_B and R_s values are given in Table 1 for both devices. The γ values were 6 and 2 for the Al/n-Si and $LiCoO_2$-interlayered device, respectively. Moreover, Φ_B and R_s values accord well with the results obtained from TE and Cheung values. Minor differences at the Φ_B and R_s values can be attributed to approximation [46].

Optical detector parameters of the Al/n-Si and Al/$LiCoO_2$/n-Si heterostructures are obtained by current transient characteristics. Photocurrent (I_p), photosensitivity (K), responsivity (R) and specific detectivity ($D*$) of the devices can be obtained by I–t plots. The I–t plots of the undoped and $LiCoO_2$-interlayered photodiodes are presented in Fig. 12. The Al/$LiCoO_2$/n-Si device clearly gave immediate and higher responses for every light power illumination compared to Al/n-Si device.

To calculate the photodetector parameters, photosensitivity (K), responsivity (R) and specific detectivity (D') equations are used, respectively, as follows.

$$I_p = I_{light} - I_{dark} \tag{14}$$

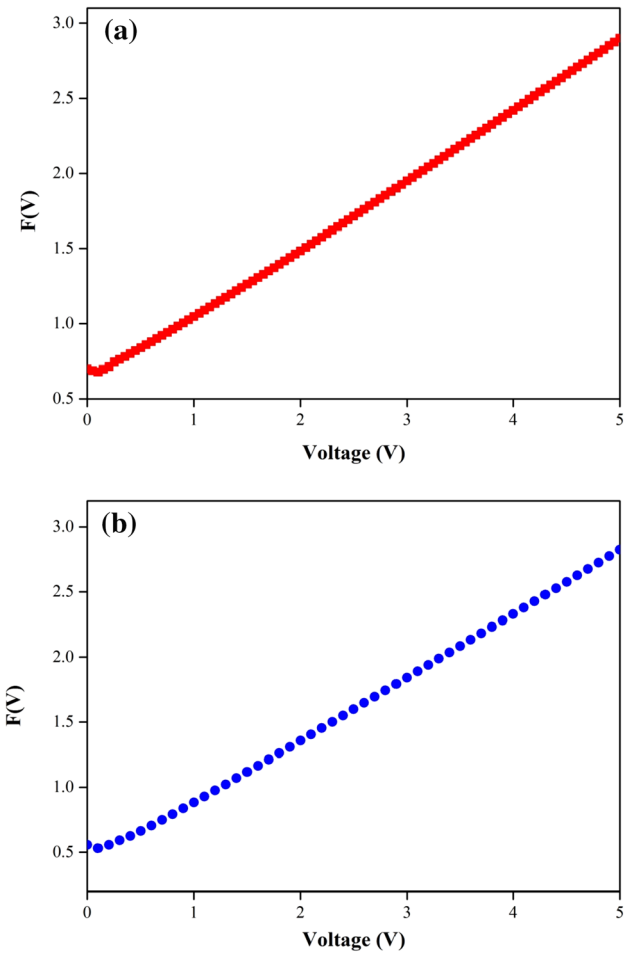

Fig. 11 Norde function plots of the **a** undoped and **b** $LiCoO_2$-interlayered photodiodes

$$K = \frac{I_p}{I_{dark}} \tag{15}$$

$$R = \frac{I_p}{PA} \tag{16}$$

$$D^* = R\sqrt{\frac{A}{2qI_{dark}}} \tag{17}$$

Here, P is symbolized of incident power density and A stands for the effective detector area. Responsivity, photosensitivity and specific detectivity values of the undoped and $LiCoO_2$-interlayered photodiodes heterostructures were calculated and are listed in Table 2. Responsivity, specific detectivity, and photosensitivity of the Al/

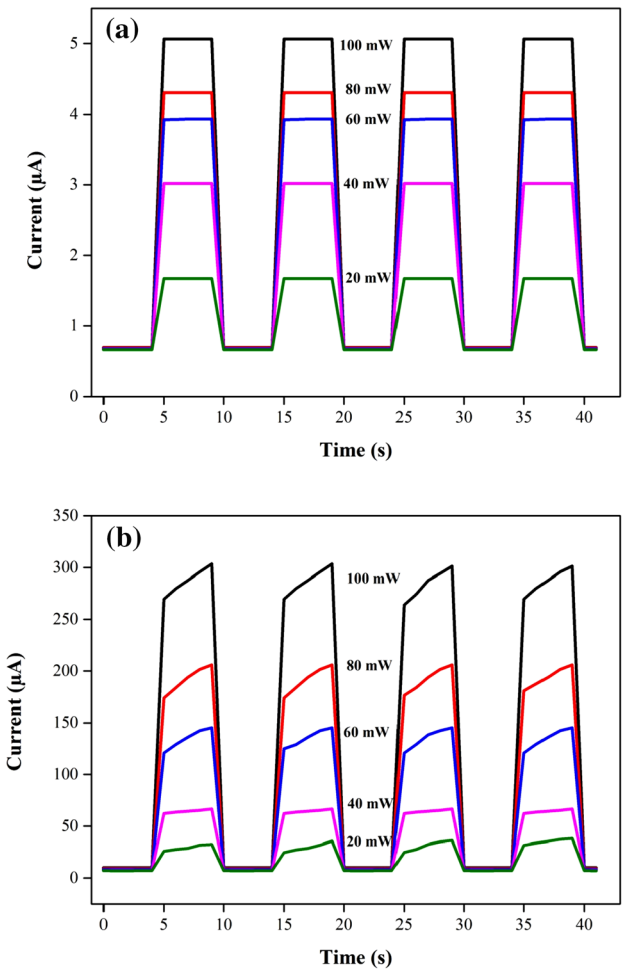

Fig. 12 *I–t* plots of the **a** undoped and **b** $LiCoO_2$-interlayered photodiodes

$LiCoO_2$/*n*-Si photodiode are considerably higher than those of Al/*n*-Si photodiode.

Photosensitivity of the undoped and $LiCoO_2$-interlayered photodiodes is shown in Fig. 13, respectively. $LiCoO_2$-interlayered device has an increasing slope with increasing light power. Furthermore, photosensitivity of both devices has an almost linear increasing profile with increasing light power.

The responsivity of the undoped and $LiCoO_2$-interlayered photodiodes is shown in Fig. 14, respectively. The Al/$LiCoO_2$/*n*-Si device showed strong responsivity values compared to Al/*n*-Si device, which are approximately 47 times higher than those of Al/*n*-Si device. Responsiveness of both devices increased as light power intensity increased.

Specific detectivity profiles of the undoped and $LiCoO_2$-interlayered photodiodes are shown in Fig. 15, respectively. The D^* values of $LiCoO_2$-interlayered device are approximately 13 times higher than those of Al/*n*-Si device, due to the addition of $LiCoO_2$ layer. The D^* values of Al/$LiCoO_2$/*n*-Si have increased with light power intensity; on the other hand, D^* values of Al/*n*-Si device have decreased by increasing light intensity.

4 Conclusion

$LiCoO_2$ was synthesized by sol–gel-based electrospinning technique. Electrospun $LiCoO_2$ nanofibers were calcinated at 650 °C at a heating rate of 10 °C/min. Calcinated $LiCoO_2$ was ball-milled and applied as interlayer between Al and *n*-type Si to fabricate Al/$LiCoO_2$/*n*-Si photodiode via ultrasonic spray pyrolysis and physical vapor deposition methods. $LiCoO_2$ was characterized via XRD, SEM

Table 2 Photodetector parameters under various illumination intensities

Devices	Power (mW/cm^2)	Photocurrent (A)	Photosensitivity –	Responsivity (A/W)	Specific detectivity (Jones)
Al/*n*-Si	20	1.01×10^{-6}	1.54	0.0064	1.24×10^{9}
	40	2.35×10^{-6}	3.53	0.0075	1.44×10^{9}
	60	3.26×10^{-6}	4.81	0.0069	1.32×10^{9}
	80	3.62×10^{-6}	5.26	0.0058	1.09×10^{9}
	100	4.37×10^{-6}	6.32	0.0056	1.05×10^{9}
Al/$LiCoO_2$/*n*-Si	20	2.47×10^{-5}	3.48	0.1570	9.24×10^{9}
	40	5.78×10^{-5}	7.69	0.1840	1.05×10^{10}
	60	1.34×10^{-4}	15.75	0.2840	1.53×10^{10}
	80	1.92×10^{-4}	20.19	0.3060	1.55×10^{10}
	100	2.86×10^{-4}	28.13	0.3640	1.79×10^{10}

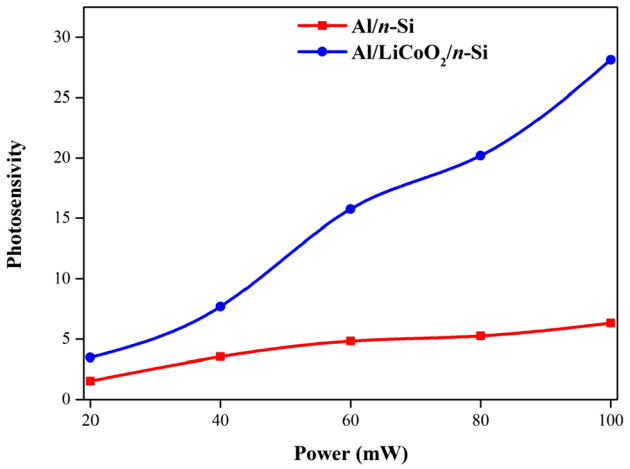

Fig. 13 Photosensitivity of the undoped and $LiCoO_2$-interlayered photodiodes

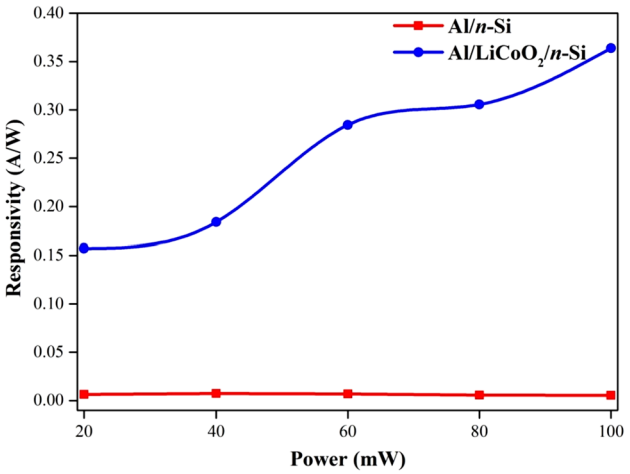

Fig. 14 Responsivity profile of the undoped and $LiCoO_2$-interlayered photodiodes

and AFM. XRD results demonstrate clear peaks of $LiCoO_2$. Moreover, AFM results accord well with SEM results. Crystallite size for $LiCoO_2$ was found to be 37.75 nm. Electrical characterization was performed under dark and various illumination conditions. $I-V$ results demonstrated that the $LiCoO_2$-interlayered device has good photodiode behavior and a high rectifying ratio. n and Φ_B values of $LiCoO_2$-interlayered device were 1.97 and 0.556, respectively. $LiCoO_2$-interlayered device has shown significant responsiveness and detectivity compared to undoped device. It has shown 1.79×10^{10} Jones detectivity and 0.364 A/W responsivity at 100 mW light power. Under dark conditions,

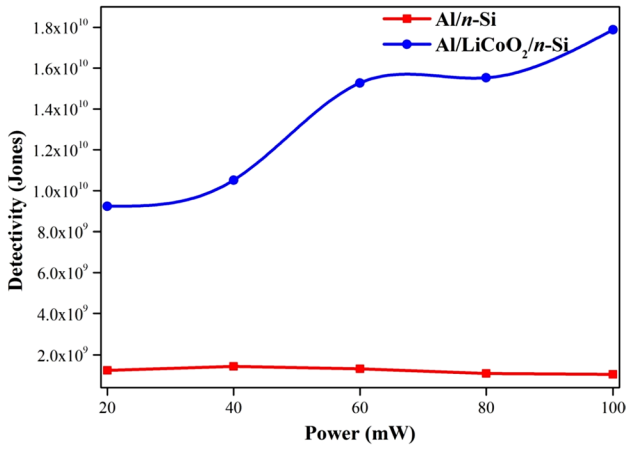

Fig. 15 Specific detectivity plots of the undoped and $LiCoO_2$-interlayered photodiodes

it demonstrated well rectifying behaviors due to reduced reverse bias and larger forward bias currents at the $I-V$. Therefore, the findings show that a device based on $LiCoO_2$ can be employed in optoelectronic applications.

Acknowledgements This work was supported by Selçuk University BAP office with 21401060 Project Number.

Data availability The datasets generated and analysed during the study are available from the corresponding author on reasonable request.

References

1. Ş Altındal, Ö. Sevgili, Y. Azizian-Kalandaragh, A comparison of electrical parameters of Au/n-Si and Au/(CoSO4–PVP)/n-Si structures (SBDs) to determine the effect of (CoSO4–PVP) organic interlayer at room temperature. J. Mater. Sci. Mater. Electron. **30**(10), 9273–9280 (2019). https://doi.org/10.1007/s10854-019-01257-5
2. S. Demirezen, S. Altındal Yerişkin, A detailed comparative study on electrical and photovoltaic characteristics of Al/p-Si photodiodes with coumarin-doped PVA interfacial layer: The effect of doping concentration. Polym. Bull. **77**(1), 49–71 (2020). https://doi.org/10.1007/s00289-019-02704-3
3. R. Siva Prakash et al., A facile fabrication of Sn-doped CeO_2 nanocrystalline thin films with enhanced photodiode properties for optoelectronic applications. Appl. Phys. A **127**(3), 173 (2021). https://doi.org/10.1007/s00339-021-04311-4
4. M. Yıldırım, A. Kocyigit, Characterization of Al/In:ZnO/p-Si photodiodes for various In doped level to ZnO interfacial layers. J. Alloys Compd. **768**, 1064–1075 (2018). https://doi.org/10.1016/j.jallcom.2018.07.295
5. S.O. Tan, H. Tecimer, O. Cicek, Comparative investigation on the effects of organic and inorganic interlayers in Au/n-GaAs Schottky diodes. IEEE Trans. Electron Devices **64**(3), 984–990 (2017). https://doi.org/10.1109/TED.2016.2647380

6. P.C.Y. Chow, T. Someya, Organic photodetectors for next-generation wearable electronics. Adv. Mater. **32**(15), 1902045 (2020). https://doi.org/10.1002/adma.201902045
7. M. Yıldırım, A. Kocyigit, Y. Torlak, E. Yenel, A.A. Hussaini, M. Kuş, Electrical behaviors of the Co- and Ni-based POMs interlayered Schottky photodetector devices. Adv. Mater. Interfaces (2022). https://doi.org/10.1002/admi.202102304
8. A. Basir et al., A novel self-powered photodiode based on solution-processed organic TPD:Alq3 active layer. Mater. Sci. Semicond. Process. **131**, 105886 (2021). https://doi.org/10.1016/j.mssp.2021.105886
9. P. Dardano, M.A. Ferrara, Integrated photodetectors based on group IV and colloidal semiconductors: current state of affairs. Micromachines **11**(9), 842 (2020). https://doi.org/10.3390/mi11090842
10. S. Yoon, K.M. Sim, D.S. Chung, Prospects of colour selective organic photodiodes. J. Mater. Chem. C **6**(48), 13084–13100 (2018). https://doi.org/10.1039/C8TC04371J
11. F. Mei et al., Recent progress in perovskite-based photodetectors: the design of materials and structures. Adv. Phys. X **4**(1), 1592709 (2019). https://doi.org/10.1080/23746149.2019.1592709
12. Z. Zhao, C. Xu, L. Niu, X. Zhang, F. Zhang, Recent progress on broadband organic photodetectors and their applications. Laser Photon. Rev. **14**(11), 2000262 (2020). https://doi.org/10.1002/lpor.202000262
13. M. Yalcin, D. Ozmen, F. Yakuphanoglu, Sr-doped yttrium nickel oxide-based photodetectors. J. Mater. Sci. Mater. Electron. **31**(4), 3441–3455 (2020). https://doi.org/10.1007/s10854-020-02892-z
14. M.M. Koç et al., Optoelectronic investigation of Cu_2FeSnS_4 quaternary functional photodiodes with IR detection capabilities. J. Mol. Struct. **1246**, 131265 (2021). https://doi.org/10.1016/j.molstruc.2021.131265
15. Y. Xia, *Polymer/Polymer Blends in Organic Photovoltaic and Photodiode Devices*, vol. 1974 (Linköping University Electronic Press, Linköping, 2019)
16. E. Yenel, Y. Torlak, A. Kocyigit, İ Erden, M. Kuş, M. Yıldırım, W- and Mo-based polyoxometalates (POM) as interlayer in Al/n–Si photodiodes. J. Mater. Sci. Mater. Electron. **32**(9), 12094–12110 (2021). https://doi.org/10.1007/s10854-021-05838-1
17. A. Kocyigit, D.E. Yıldız, A. Sarılmaz, F. Ozel, M. Yıldırım, The dielectric performance of Au/CuCo5S8/p-Si heterojunction for various frequencies. J. Mater. Sci. Mater. Electron. **31**(24), 22408–22416 (2020). https://doi.org/10.1007/s10854-020-04742-4
18. A. Kocyigit, M. Yilmaz, S. Aydogan, Ü. İncekara, H. Kacus, Comparison of n and p type Si-based Schottky photodiode with interlayered Congo red dye. Mater. Sci. Semicond. Process. **135**, 106045 (2021). https://doi.org/10.1016/j.mssp.2021.106045
19. S. Karadeniz, D.E. Yıldız, H.H. Gullu, D.A. Kose, A.A. Hussaini, M. Yıldırım, Dark and illuminated electrical characteristics of Schottky device with Zn-complex interface layer. J. Mater. Sci. Mater. Electron. **33**(22), 18039–18053 (2022). https://doi.org/10.1007/s10854-022-08664-1
20. A. Kocyigit, A.A. Hussaini, M. Yıldırım, D.A. Kose, D.E. Yıldız, Schottky type photodiodes with organic Co-complex and Cd-complex interlayers. Appl. Organomet. Chem. (2022). https://doi.org/10.1002/aoc.6879
21. H.E. Lapa, A. Kökce, A.F. Özdemir, İ Uslu, Ş Altindal, A comparative study on dielectric behaviours of Au/(Zn-doped PVA)/n-4H-SiC (MPS) structures with different interlayer thicknesses using impedance spectroscopy methods. Bull. Mater. Sci. **41**(3), 82 (2018). https://doi.org/10.1007/s12034-018-1602-6
22. A. Eroğlu, S. Demirezen, Y. Azizian-Kalandaragh, Ş Altındal, A comparative study on the electrical properties and conduction mechanisms of Au/n-Si Schottky diodes with/without an organic interlayer. J. Mater. Sci. Mater. Electron. **31**(17), 14466–14477 (2020). https://doi.org/10.1007/s10854-020-04006-1
23. M.A. Butt, Thin-film coating methods: a successful marriage of high-quality and cost-effectiveness—a brief exploration. Coatings **12**(8), 1115 (2022). https://doi.org/10.3390/coatings12081115
24. S. Rahemi Ardekani, A. Sabour Rouh Aghdam, M. Nazari, A. Bayat, E. Yazdani, E. Saievar-Iranizad, A comprehensive review on ultrasonic spray pyrolysis technique: mechanism, main parameters and applications in condensed matter. J. Anal. Appl. Pyrolysis **141**, 104631 (2019). https://doi.org/10.1016/j.jaap.2019.104631
25. C.R. Michel, M.A. Lopez-Alvarez, A.H. Martínez-Preciado, Novel UV sensing and photocatalytic properties of nanostructured $LiCoO_2$ prepared by the coprecipitation method. J. Photochem. Photobiol. A Chem. **403**, 112842 (2020). https://doi.org/10.1016/j.jphotochem.2020.112842
26. Y. Ou, J. Wen, H. Xu, S. Xie, J. Li, Ultrafine $LiCoO_2$ powders derived from electrospun nanofibers for Li-ion batteries. J. Phys. Chem. Solids **74**(2), 322–327 (2013). https://doi.org/10.1016/j.jpcs.2012.10.007
27. M.O. Erdal, M. Koyuncu, İ Uslu, The effect of synthesis technique on thermoelectric properties of nanocrystalline $NaCo_2O_4$ ceramics. J. Nanoparticle Res. **16**(11), 2715 (2014). https://doi.org/10.1007/s11051-014-2715-5
28. W. Kern, D.A. Puotinen, Cleaning solutions based on hydrogen peroxide for use in silicon semiconductor technology. RCA Rev. **31**, 187–206 (1970)
29. S. Ruzgar, M. Caglar, Fabrication and characterization of solution processed Al/Sn:ZnO/p-Si photodiodes. Mater. Sci. Semicond. Process. **115**, 105076 (2020). https://doi.org/10.1016/j.mssp.2020.105076
30. W. Yu et al., High-performance calcium-doped zinc oxide thin-film transistors fabricated on glass at low temperature. Jpn. J. Appl. Phys. **55**(4S), 04EK05 (2016). https://doi.org/10.7567/JJAP.55.04EK05
31. S. Ruzgar, Y. Caglar, O. Polat, D. Sobola, M. Caglar, The tuning of electrical performance of Au/(CuO:La)/n-Si photodiode with La doping. Surf. Interfaces **21**, 100750 (2020). https://doi.org/10.1016/j.surfin.2020.100750
32. K. Wu et al., Improving the cycling performance, rate capacity, and thermal stability of $LiCoO_2$ by doping high-valence ions into the Li+ site. J. Solid State Electrochem. **22**(12), 3725–3734 (2018). https://doi.org/10.1007/s10008-018-4046-4
33. L.A. Montoro, Changes in the electronic structure of chemically deintercalated LiCoO[sub 2]. Electrochem. Solid-State Lett. **3**(9), 410 (1999). https://doi.org/10.1149/1.1391162
34. H. Wang, Y. Jang, B. Huang, D.R. Sadoway, Y. Chiang, TEM study of electrochemical cycling-induced damage and disorder in $LiCoO_2$ cathodes for rechargeable lithium batteries. J. Electrochem. Soc. **146**(2), 473–480 (1999). https://doi.org/10.1149/1.1391631
35. D.D.M. Prabaharan, K. Sadaiyandi, M. Mahendran, S. Sagadevan, Precipitation method and characterization of cobalt oxide nanoparticles. Appl. Phys. A **123**(4), 264 (2017). https://doi.org/10.1007/s00339-017-0786-8
36. M.C.G. Merino, M. Palermo, R. Belda, M.E.F. de Rapp, G.E. Lascalea, P.G. Vázquez, Combustion synthesis of Co_3O_4 nanoparticles: Fuel ratio effect on the physical properties of the resulting powders. Procedia Mater. Sci. **1**, 588–593 (2012). https://doi.org/10.1016/j.mspro.2012.06.079
37. H. Cavusoglu, Structural, morphological and optical studies of nanostructured cadmium oxide films: the role of pH. J. Mater. Sci. Mater. Electron. **29**(15), 12777–12784 (2018). https://doi.org/10.1007/s10854-018-9396-2

38. M. Yildirim, Determination of contact parameters of Au/n-Ge Schottky barrier diode with rubrene interlayer. Politek. Derg. **20**(1), 165–173 (2017)
39. S. Sen, N.B. Manik, Correlation between barrier potential and charge trapping under the influence of titanium di oxide nanomaterials in organic devices. Results Mater. **8**, 100145 (2020). https://doi.org/10.1016/j.rinma.2020.100145
40. P. Li, B.N. Shivananju, Y. Zhang, S. Li, Q. Bao, High performance photodetector based on 2D $CH_3NH_3PbI_3$ perovskite nanosheets. J. Phys. D. Appl. Phys. **50**(9), 094002 (2017). https://doi.org/10.1088/1361-6463/aa5623
41. Ö. Vural, Y. Şafak, Ş Altındal, A. Türüt, Current–voltage characteristics of Al/Rhodamine-101/n-GaAs structures in the wide temperature range. Curr. Appl. Phys. **10**(3), 761–765 (2010). https://doi.org/10.1016/j.cap.2009.09.011
42. M. Yıldırım, A. Kocyigit, A. Sarilmaz, S.S. Ozel, M. Kus, F. Ozel, Ternary $CuCo_2S_4$ thiospinel nanocrystal-coated photodiode with improved photoresponsivity and acceptance angles for optoelectronic applications. J. Electron. Mater. **49**(2), 949–958 (2020). https://doi.org/10.1007/s11664-019-07841-z
43. S.K. Cheung, N.W. Cheung, Extraction of Schottky diode parameters from forward current-voltage characteristics. Appl. Phys. Lett. **49**(2), 85–87 (1986). https://doi.org/10.1063/1.97359
44. S. Sen, N.B. Manik, Effect of different sized multi walled carbon nanotubes on the barrier potential and trap concentration of malachite green dye based organic device. Adv. Mater. Sci. **20**(4), 16–26 (2020). https://doi.org/10.2478/adms-2020-0019
45. H. Norde, A modified forward I–V plot for Schottky diodes with high series resistance. J. Appl. Phys. **50**(7), 5052–5053 (1979). https://doi.org/10.1063/1.325607
46. M. Yilmaz, A. Kocyigit, B.B. Cirak, H. Kacus, U. Incekara, S. Aydogan, The comparison of Co/hematoxylin/n-Si and Co/hematoxylin/p-Si devices as rectifier for a wide range temperature. Mater. Sci. Semicond. Process. **113**, 105039 (2020). https://doi.org/10.1016/j.mssp.2020.105039